

IFU Unit in SCORPIO-2 Focal Reducer for Integral-Field Spectroscopy on the 6-m Telescope of the SAO RAS

V.L. Afanasiev ^{1,*}, O.V. Egorov ^{2,1}, A.E. Perepelitsyn ¹

ABSTRACT

We describe the scheme and design features of the new IFU unit (Integral Field Unit) meant to perform integral-field spectroscopy as a part of SCORPIO-2 focal reducer, which is mounted in the prime focus of the 6-m telescope of the Special Astrophysical Observatory of the Russian Academy of Sciences. The design of the unit is based on the principle of the formation of array spectra using a lens raster combined with optical fibers. The unit uses a rectangular raster consisting of 22×22 square 2-mm diameter lenses. The image of the object is transferred by an optical system with a $23\times$ magnification from the focal plane of the telescope to the plane of the lens raster. The image scale is $0''.75/\text{lens}$ and the field of view of the instrument has the size of $16''.5 \times 16''.5$. The raster also contains two extra 2×7 lens arrays to acquire the night-sky spectra whose images are offset by $\pm 3'$ from the center. Optical fibers are used to transform micropupil images into two pseudoslits located at the IFU collimator entrance. When operating in the IFU mode a set of volume phase holographic gratings (VPHG) provides a spectral range of 4600–7300 Å and a resolution $\lambda/\delta\lambda$ of 1040 to 2800. The quantum efficiency of SCORPIO-2 field spectroscopy is 6–13% depending on the grating employed. We describe the technique of data acquisition and reduction using IFU unit and report the results of test observations of the Seyfert galaxy Mrk 78 performed on the 6-m telescope of the Special Astrophysical Observatory of the Russian Academy of Sciences.

Subject headings: instruments: spectrograph—techniques: data analysis—techniques: spectroscopic—techniques: image spectroscopy

1. INTRODUCTION

Currently, most of the major telescopes are equipped with integral-field spectrographs (IFS) designed for field spectroscopy. The IFS concept was proposed by Courtés (1982) and published by Vanderriest et al. (1984). Various spectrograph versions were first made by Bacon et al. (1995); Arribas et al. (1990); Afanasiev et al. (1990). In the past century many astronomers viewed field spectroscopy as a methodologically complicated technique applicable only to a limited class of tasks

limited by the small field of view of such spectrographs. The new technological advances of recent decades resulted in the creation of efficient IFS designed for a wide range of tasks, which we do not list here as this is beyond the scope of this paper. We only mention dedicated spectrographs used extensively in the last decades—GMOS (Murray et al. 2003) and MUSE (Laurent et al. 2006) for 8-m telescopes and SAURON (Bacon et al. 2001) and PMAS (Roth et al. 2005) for 3–4-m diameter telescopes.

The first version of IFS used on the 6-m telescope and called MPFS (Multi Pupil Field Spectrograph) was made in 1989 (Afanasiev et al. 1990). Various modifications of this spectrograph were used successfully on the telescope until 2009 and more than 100 papers dedicated to the study of galaxies of various types and Galactic gaseous

¹Special Astrophysical Observatory (SAO), Russian Academy of Sciences, Nizhnii Arkhyz, 357147 Karachai-Cherkessian Republic, Russia

²Sternberg Astronomical Institute, M. V. Lomonosov Moscow State University, Moscow, 119234 Russia

*E-mail: vafan@sao.ru

nebulae were published based on the results of observations made with this instrument. A description of the last version of the spectrograph can be found in Afanasiev et al. (1995, 2001). The main shortcoming of this instrument was its low transmission (DQE<5%) due to the use of the mirror-lens camera. Currently the instrument is being redesigned—we plan to mount a lens camera in it and increase transmission by a factor of 5–6.

A new multi-mode SCORPIO spectrograph has been operated at the 6-m telescope since 2000 (Afanasiev & Moiseev 2005). The instrument implements image-acquisition mode, long-slit spectroscopy, multi-object spectroscopy, spectropolarimetry, and field spectroscopy performed using a scanning Fabry–Perot interferometer (FPI). Our desire to expand its capabilities and transition to a larger-format detector motivated us to begin in 2010 a project aimed at creating the new multi-mode SCORPIO-2 spectrograph (Afanasiev & Moiseev 2011). A description of the already implemented capabilities of this spectrograph can be found on the WEB page of the project¹. The new instrument provides field spectroscopy mode and this paper describes the IFU mode of SCORPIO-2 spectrograph: design, technique of data acquisition, and the first results obtained on the 6-m telescope.

2. OPTICAL LAYOUT

SCORPIO-2 focal reducer is mounted in the prime focus of the 6-m telescope of the Special Astrophysical Observatory of the Russian Academy of Sciences. Unlike most of the field spectrographs of major telescopes, which are mounted in the secondary foci and have entrance focal ratios $<F/8$, SCORPIO-2 has an entrance focal ratio of $F/4$. This circumstance imposes important constraints on the design features of the integral-field unit of IFU given the small size of the spectrograph, which was limited by the volume of the prime focus cabin. The front segment of SCORPIO-2 (the distance from the mounting plane of the turret to the slit) is equal to 38 mm, preventing the implementation of technical solutions like GMOS (Murray et al. 2003) and PMAS (Roth et al. 2005). We found a solution, which allows mounting the

IFU unit in the spectrograph case while preserving the possibility of fast switching between operating modes. Our solution is based on the principle of the use of a lens raster combined with optical fibers suggested by Courtés (1982), which we were the first to implement on the 6-m telescope (Afanasiev et al. 1990). Unlike Roth et al. (2005), we use short fibers with the length of 140–150 mm, which allowed us to accommodate the IFU unit inside the spectrograph. This solution reduced the light losses and minimized variations of fiber transmission due to flexure variations. In the IFU we use another collimator, which is introduced into the beam instead of the collimator used for the focal reducer. We show the optical layout of the spectrograph operating in the IFU mode in Fig. 1. The camera of the spectrograph (6-lens apochromat, $F = 109$ mm, $F/2.6$, $2\omega = 36^\circ$) is used in all modes and produces the image at the entrance of the 4600×2048 px² EEV42-90 CCD (1 px = $13.5 \mu\text{m}$). The collimator of the IFU unit (5-lens achromat, $F = 240$ mm, $F/6$, $2\omega = 22^\circ$) is focal-ratio matched with the entrance aperture of optical fibers. To reduce the size, we use a solution where the fiber unit is located inside the collimator, which has 60×80 mm² holes in the last three lenses. Two 56-mm long pseudoslits are projected by the collimator and camera onto the detector plane. The distance between the slit centers is equal to 66 mm. The volume phase holographic grating (VPHG) forms two arrays of spectra in the detector format. The working portion of the spectrum of each grating is selected by the interference band filter introduced into the beam after the magnifier lens.

Fig. 2 gives the idea of the principle of operation of the IFU mode of the spectrograph. Panel (a) shows the optical layout of the formation of the image on the lens raster. The central negative lens projects the magnified image of the field studied from the focal plane of the primary mirror of the 6-m telescope onto the focal plane of the lens raster. We use a lens raster consisting of a 22×22 array of 2×2 mm² rectangular lenses with a focal distance of 13.5 mm. Image magnification in our case is $23\times$, resulting in the image scale of $0''.75/\text{lens}$ and a $16''.5 \times 16''.5$ field of view. The other two lenses mounted at a distance of ± 20 mm from the center ($\pm 3'$) project images of night-sky portions onto 2×7 lens rasters. To meet the telecentric-

¹<http://www.sao.ru/hq/lsvfo/devices/scorpio-2/index.html>

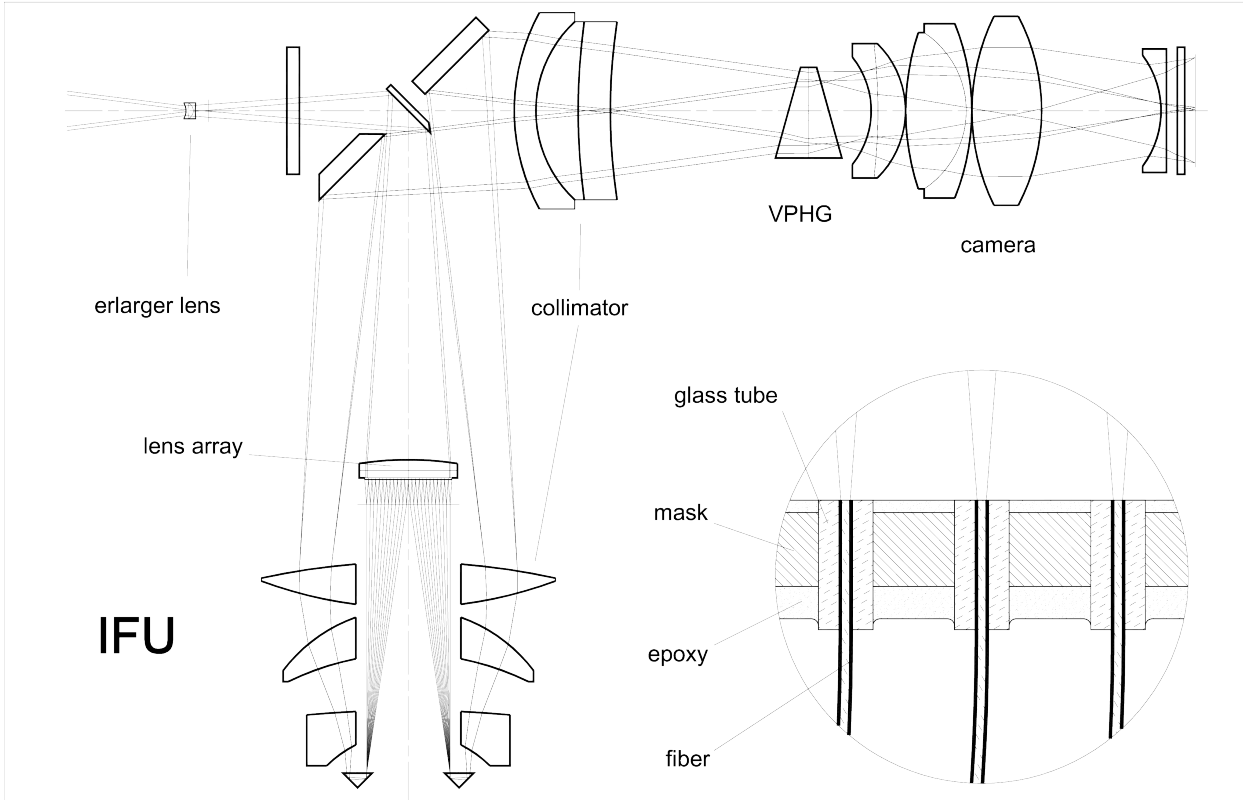


Fig. 1.— Optical scheme of IFU mode in SCORPIO-2 spectrograph. The inset image shows the lens raster unit and fibers.

ity condition, field lenses are mounted in front of each lens raster. Fig. 2b shows the photo of a lens raster. Each lens forms a $150\text{-}\mu\text{m}$ diameter image of the telescope mirror (a micropupil).

The resulting array of micropupils is transferred onto two pseudoslits via optical fibers. Fig. 2e shows the spectra of the calibrating source (the continuum and line spectrum are produced by a quartz and Ar-Ne-He filled lamp, respectively) from two pseudoslits. The pseudoslit is reformed so that the columns of one half of the array of micropupils would be arranged sequentially along the slit in groups of 22 micropupils separated by images of micropupils from night-sky portions. Figs. 2c and d demonstrated this arrangement in a magnified fragment of a portion of IFU spectra.

2.1. Lens Raster with Optical Fibers

Let us now consider in more detail the design of the unit of lens raster and fibers. To reform the

micropupil array, we use a custom-made optical fiber that ordered from “Forc-Photonics group”² with the following parameters:

- Number aperture— 0.10 ± 0.01 ;
- Core material—quartz glass with high OH concentration, clear aperture $150\ \mu\text{m}$;
- Coating material—doped quartz glass, diameter $165\ \mu\text{m}$;
- Protective coating—Al, diameter $195\text{--}200\ \mu\text{m}$.

As we pointed out above, the size of the micropupil in our case is $150\ \mu\text{m}$, and the maximum aperture of the converging beam after each lens corresponds to the F/4 focal ratio and matches the entrance aperture of the fiber. It is clear that inaccurate placement of fibers in micropupil positions would result in the loss of transmission. Precise placement of fibers is a well-known problem (Roth et

²<http://www.forc-photonics.ru/>

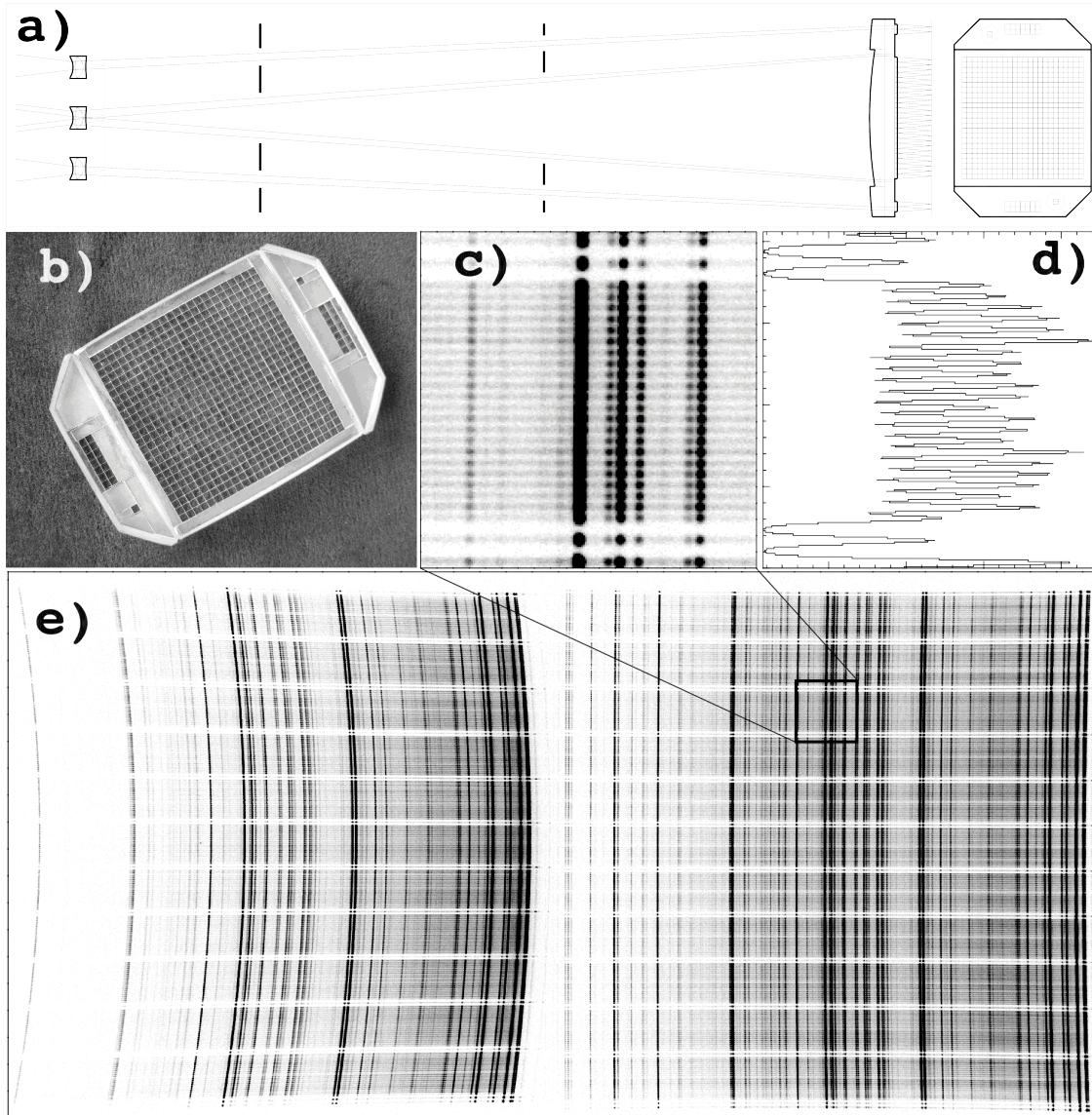


Fig. 2.— Lens raster of SCORPIO-2 IFU: (a) optical layout of the image formation and (b) appearance. Examples of spectra acquired in the IFU mode: (c) selected image fragment, (d) cross section made across the direction of dispersion, (e) images of the spectra of the calibrating source (see text for details).

al. 2005), which has several solutions. In our case we preinstalled the IFU unit on the telescope and obtained a photographic image of the micropupil array. We measured the micropupil positions on the photographic plate and then made a mask with 805–810- μm -diameter holes, where we put capillary glass pipes with the inner and outer diameter of 205–215 and 780–790 μm , respectively. We put one end of the fiber into these pipes and the other end, into the 205 μm -wide gap between two glass plates (see the inset image in Fig. 1), and fixed them with optical glue. We then poured epoxy plastic glue onto the fibers with piles, and polished the fiber ends on both sides. Note that such technology ensures high quality of fiber end processing and, as a result, low Fresnel losses at the entrance and exit of the fibers. After optical processing and mounting the unit into the case we measured the fiber positions. The results are shown in Fig. 3.

As is evident from the figure, transmission, which is determined by the error of fiber placement, is of about 90%. The actual transmission also depends on Fresnel losses on optical surfaces (in our case they are less than 15%) and chromatic aberrations of the raster. Computations show that the 150 mm diameter circle concentrates at least 85% of the diameter of the polychromatic micropupil image. We can thus conclude that the transmission of the lens raster is no less than 65%. The mechanical structure of the unit allows adjusting the position of the lens raster relative to the fiber array using micrometric screws. Adjustment control on the telescope can also be performed

2.2. VPHG in the IFU Mode Operation Features

Volume phased holographic gratings with direct viewing prisms are used as dispersing elements in SCORPIO-2 focal reducer. The VPHG used in astronomy have high transmission and low scattered light (Barden et al. 2000). If φ is the angle at the prism apex and θ , the angle between the optical axis and the axis of the collimated beam, then the incidence angle onto the grating, α , can be found from formula $\sin(\varphi - \theta) = n_p \sin(\varphi - \alpha)$, where n_p is the refractive index of the prism material. When operating in the common spectroscopy mode $\theta = 0$ (the beam is parallel to the optical axis), while $\theta \neq 0$ in the IFU mode. It leads to the difference in the efficiency of VPHG for different slits.

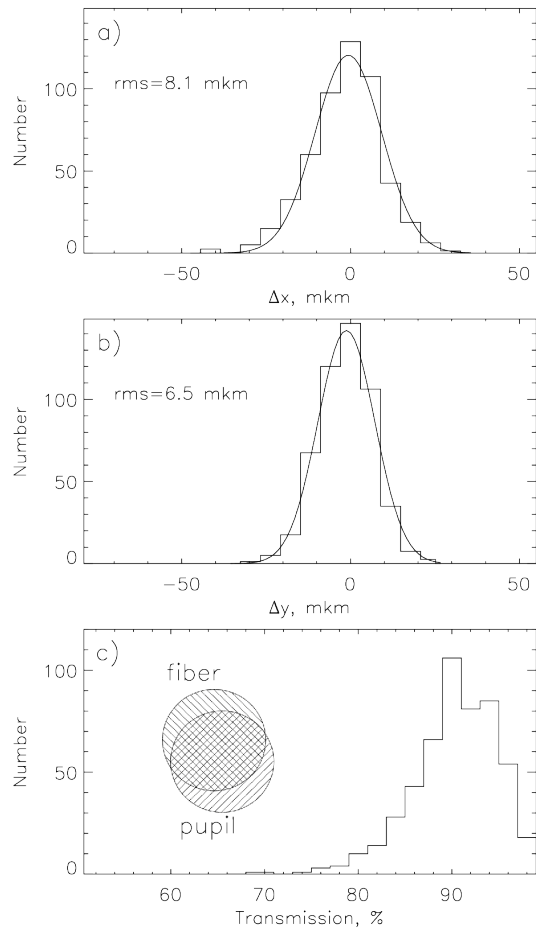


Fig. 3.— Transmission losses of the fiber-lens IFU unit due to incorrect mounting of the fibers: (a) and (b)—the distributions of errors along the X and Y -axes, (c)—Distribution of fiber transmission, the mean value is $91.5 \pm 3.3\%$.

In the Kogelnik approximation (Kogelnik 1969) the efficiency of the grid in the case of given incidence angle α and wavelength λ is given by the following formula:

$$\eta(\lambda) = \frac{1}{2} \sin^2 \Psi + \frac{1}{2} \sin^2(\Psi \cos(\alpha + \beta(\lambda))), \quad (1)$$

$$\text{where } \Psi = \frac{\pi \Delta n_g d_g}{\lambda \cos \alpha}.$$

Here d_g is the thickness of the gelatine layer of the grating; Δn_g , the amplitude of modulation of the refractive index n_g of the layer, and $\beta(\lambda)$, the scattering angle for light with wavelength λ onto the

grating plane. The efficiency of the grating reaches maximum at wavelength λ_{\max} if $\alpha = \beta(\lambda_{\max})$. In this case angle α is called the Bragg angle and the following condition is satisfied:

$$\lambda_{\max} \nu_g m = n_g \sin(\alpha), \quad (2)$$

where ν_g is the frequency of modulation of the refractive index of the grating and m , the order of scattering, which is equivalent to the diffraction order of ordinary gratings. Note that in this case $1/\nu_g$ is equivalent to the number of lines in ruled gratings; α , to the blaze angle, and $\beta(\lambda)$, to the diffraction angle. Angles between collimated beams in the IFU and the optical axis (see Fig. 1) are equal to $\pm 8^\circ$. Fig 4 shows the efficiency curves for VPHG1200@540 grating, which has a maximum of concentration at $\lambda = 5400 \text{ \AA}$ and $1/\nu_g = 1200 \text{ mm}^{-1}$, computed by formula (1). We performed our computations adopting the following values for the grating parameters: $n_g = 1.582$, $\Delta n_g = 0.0286$, and $d_g = 10.15 \text{ \mu m}$, and the Bragg angle of $19^\circ 2$ in air. We used a prism made of LK-8 ($n_p = 1.473$) glass with angle $\varphi = 36^\circ$. As is evident from the figure, theoretical efficiency curves differ significantly for different slits—on the average (this corresponds to the middle of the range) efficiency of the VPHG when operating in IFU mode decreases by a factor of about 1.5 compared to the long-slit (LS) mode. Note that in the case of “left” ($\theta = +8^\circ$) and “right” ($\theta = -8^\circ$) slit efficiency increases and decreases with wavelength, respectively.

To test this conclusion, we compared the spectral fluxes from quartz lamp in IFU mode with the corresponding fluxes in LS mode for VPHG1200@540 grating available in SCORPIO-2. We used the data about the spectrograph efficiency in the LS mode with the account for spectral sensitivity of the CCD and transmission of the optics of SCORPIO-2 (Afanasiev & Moiseev 2011). We compared not only the difference between the efficiency of VPHG in different modes, but also the difference between the transmission of optics, which included the transmission of the linear raster with light-emitting diodes. Fig. 4b shows the result of a comparison of real spectral transmission for each slit in the IFU and LS modes. As is evident from the figure, the efficiency of IFU mode at the center of the spectral range decreases, on the average, by a factor of 2.5 com-

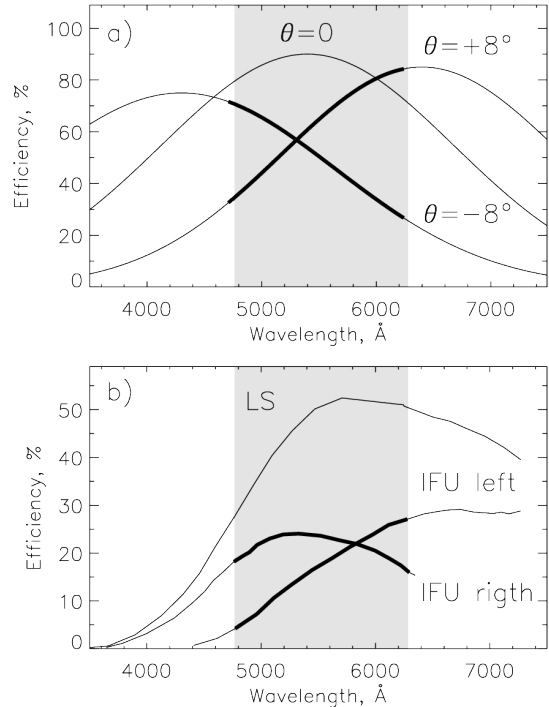


Fig. 4.— Calculated (a) and observed (b) effectiveness of the VPHG1200@540 grating operating in IFU mode. Gray color is used to indicate the spectral interval selected by the interference filter for this grating, 4900–6150Å.

pared to the LS mode. Given the transmission of the lens raster with light-emitting diodes, which is on the order of 60–65%, this estimate agrees with our computations.

The parameters of the grating used in the IFU mode are listed in the Table. It gives: grating name (the number in front of the @ symbol indicates the number of lines; the next numbers indicate the wavelength of maximum concentration in nm, spectral range selected by the filter in \AA px^{-1} , and resolution limits $\lambda/\delta\lambda$ computed by the measured widths of lines.

2.3. Variations of Resolution and Flexure of the Spectrograph when Operated in the IFU Mode

The stability of resolution (PSF) across the entire recorded field in the IFU mode is one of the most important properties of the instrument. Variations of the line halfwidths in the spectra

Table 1: Parameters of gratings in the IFU mode

Grating	Spectral coverage, Å	Dispersion, Å px ⁻¹	Resolution, λ/δλ
VPHG940@600	4700–7300	0.90–1.15	1044–1269
VPHG1200@540	4800–6150	0.81–0.90	1186–1351
VPHG1800@510	4600–5400	0.40–0.50	1957–2118
VPHG1800@590	5700–6500	0.41–0.51	2375–2453
VPHG1800@660	6300–7100	0.42–0.52	2571–2582
VPHG2300@520	4930–5630	0.30–0.40	2739–2815

formed by individual light-emitting diodes should be small and vary smoothly across the field of view. This primarily determines the success of the subtraction of the night-sky spectrum. Variation of widths across the dispersion affects the quality of the extraction of spectra and hence spectral reproducibility. Fig. 5 shows measured FWHM determined from monochromatic images of individual light-emitting diodes in the spectrum of neon. The spectrum was acquired with VPHG1800@660 grating in the 6300–7100 Å wavelength range, where many bright lines are recorded. Fig. 5a shows the variations of the FWHM of lines along the dispersion. Note that the scatter of data points is determined by measurement errors. The increase of FWHM at the edges is determined by the smooth variation of the angular magnification of the grating and by the decrease of the camera resolution at the edge of the field of view. The first circumstance results in appreciable change of the dispersion on the left slit from 0.52 Å px⁻¹ to 0.40 Å px⁻¹, which translates into a change of the line profile in velocity scale from 110 km s⁻¹ to 120 km s⁻¹. Such changes are acceptable for most of the tasks that require an analysis of the line profiles of the objects studied. There are no variations of the profile width along the pseudoslit (Fig. 5b) within the measurement errors. This result is important for choosing algorithms for extraction of spectra and offers hope for the realization of good photometric stability of the IFU mode.

Flexures occur in every instrument mounted in the moving focus of the telescope. Measurement SCORPIO-2 flexures in the LS mode demonstrate high position stability of the instrument—they do not exceed 0.8 px (about 10 μm) in the $z = 5^\circ$ – 60° interval of zenith angles. A special feature of the IFU mode is that only a part of the collimator — a three-lens assembly and a diagonal mirror — is

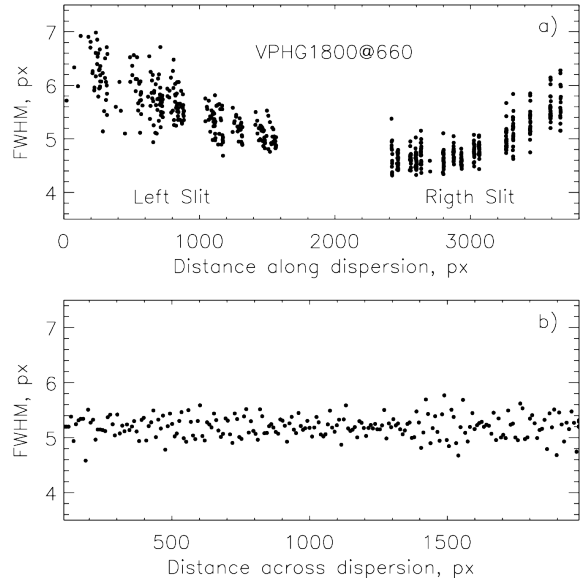


Fig. 5.— Variations of the widths of lines in the comparison spectrum in the IFU mode for VPHG1800@660 grating: (a) along and (b) across the dispersion.

introduced into the beam. The last three lenses of the collimator, which are located in the same case with the fiber-lens unit, are fixed and do not move. In the case of the change of the zenith angle and rotation of the instrument this results in the shift of the line positions. Flexure measurements in the IFU mode (Fig. 6) show that during a 15–20 min exposure the image shift does not exceed 0.3 pix and does not degrade the resolution. Given the structure of each image (intensity “modulations” both along the dispersion and along the pseudoslit), flexure effects are easy to take into account—during reduction of our data each image is reduced to the unified reference frame to within 0.1 px.

3. REDUCTION OF OBSERVATIONAL DATA

A complete data set acquired during SCORPIO-2 observations with IFU includes:

- Bias frames (BIAS), which are usually taken at the beginning and at the end of the night;
- Flatfield spectrum (FLAT); it is taken immediately before and after the observations of the

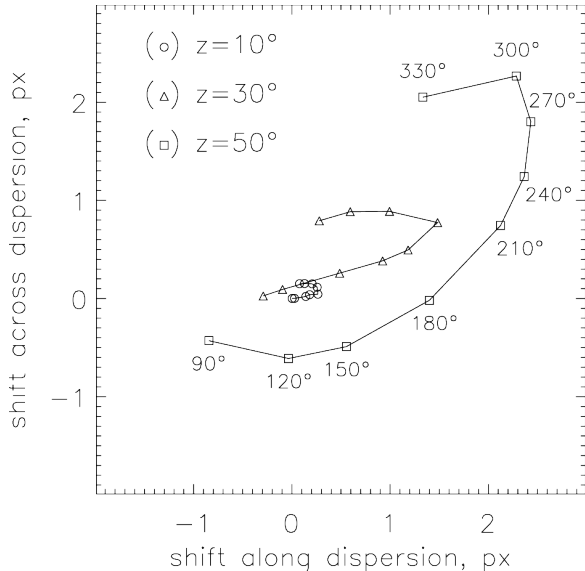


Fig. 6.— Flexures of SCORPIO-2 in the IFU mode at different zenith angles and in the case of the rotation of the instrument. For shifts measured at zenith angle 50° the corresponding turret angles are indicated.

object;

- Standard spectrum (ETA) obtained by illuminating 12dots mask with flatfield lamp and which reflects the position of spectra from “sky” fibers in the frame; it is taken once before and once after the observation of the object;
- Comparison spectrum of the He-Ne-Ar calibrating lamp (NEON); like FLAT, it is taken before and after observations of the object;
- Spectra of the observed object (OBJ); at least three exposures should be taken to remove cosmic-ray hits;
- Spectra of spectrophotometric standard (STAR) taken shortly before or after observations of the object at a similar zenith angle;
- Twilight sky spectra (SUNSKY); taken in the evening before sunset and in the morning before sunrise.

We reduce observational data using standard procedures employed in 3D spectroscopy. Any programs for the analysis of the data from IFU spectrographs can be used (e.g., p3D, Sandin et al. 2010). We prefer our own package written in

IDL. All reduction stages in IFURED take into account specific features of the data obtained with IFU unit in SCORPIO-2.

Fig. 7 shows raw frames of various types: (a) OBJ, (b) NEON, (c) ETA, and (d) FLAT. During our test observations no SUNSKY has been taken and we therefore do not show its example and do not consider it in our description of the data reduction procedure.

As is evident from Fig. 7, the spectra from the left and right slits overlap approximately at the center of the frame. Furthermore, during observations with VPHG940@600 grating the second order of the spectrum obtained from the right slit (the effect is especially apparent in the ETA images, Fig. 7c). In this connection when reducing the data we fix the boundaries of the spectra from the right and left slits on the acquired frames trimming cutting the overlap areas.

Below in this section we describe the main stages of reduction using IFURED package³. Fig. 8 shows the flowchart diagram of the IFU data reduction procedure, which has the form of a sequence of actions. As an example let us consider the data acquired with VPHG940@600 grating for the Mrk 78 galaxy.

3.1. Assembly of Initial 2D Spectra

At the initial stage we average all available BIAS frames and subtract the resulting MEANBIAS frame from all individual exposures.

We then apply corrections to take into account possible offsets (which may be caused by flexures inside the instrument) between different exposures both within the same set and between different types of data. We first use cross-correlation to determine the offset in the direction perpendicular to dispersion between individual exposures of the object and shift all frames to align them with the first exposure. We then use a similar procedure to determine the offset between the flatfield and object spectra and then align all the remaining frames with the flatfield spectrum. For some OBJ, NEON, and STAR exposures we also determine the

³Given possible important changes in the algorithm of the program after the publication of this paper we advice the reader to read its description at the site of the project: <http://www.sao.ru/hq/lsvfo/devices/scorpio-2/index.html>

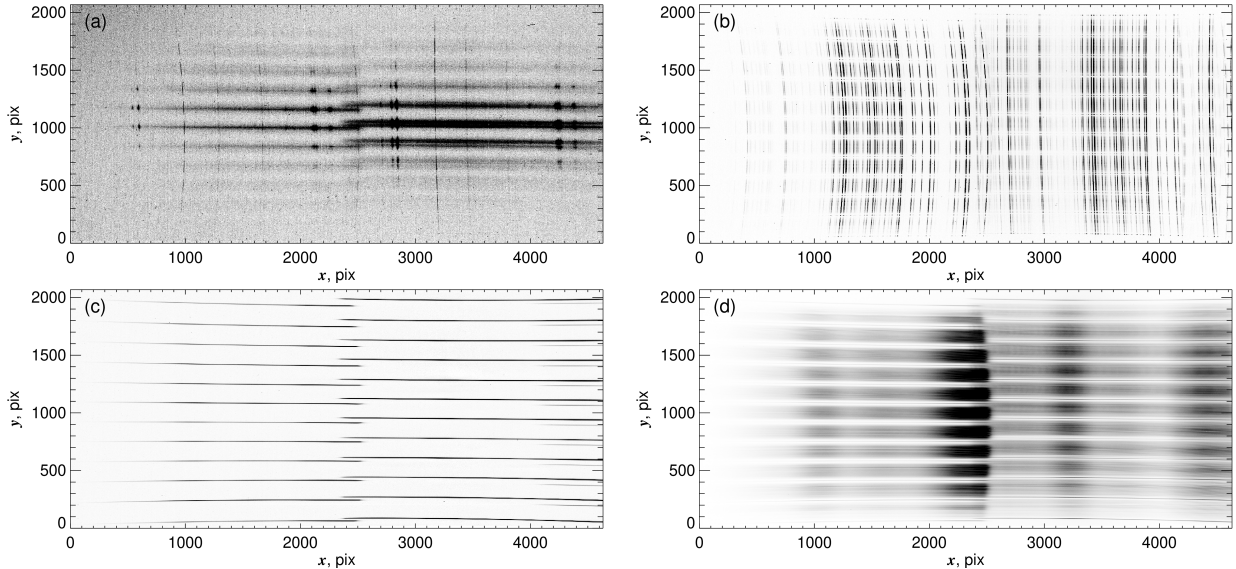


Fig. 7.— Example of raw frames from the data set acquired with VPHG940@600 grating: (a) OBJ—the spectrum of Mrk 78; (b) NEON—the calibration spectrum of the He-Ne-Ar lamp ; (c) ETA—the standard spectrum acquired with 12dots mask; (d) FLAT—the flatfield spectrum.

offsets along the dispersion and correct them. In practice offsets usually do not exceed 1 pixel, but greater offsets may occur between the STAR frame and the remaining set of data, because spectrophotometric standard frame is take at another, albeit similar, position of the telescope.

We stack individual exposures of each data type in pairs. In the process, cosmic-ray hits are removed. In each frame of the pair pixels are found where the signal significantly exceeds the number of counts in the same pixel in the other frame and intensities in these pixels are replaced by the counts from the other frame of the pair.

At this stage the spectra from the right and left slits are separated and the data cube is created with two channels along the spectral axis. Each channel contains the spectrum from the right or left slit. The spectra are then reduced separately using identical procedure.

3.2. Correction of Geometric Distortions

The next stage consists in the construction of a geometric model of the trajectories of spectra from individual fibers in the frame. The standard spectrum ETA and the calibration spectrum of the He-Ne-Ar lamp NEON are analyzed.

First, the program searches for trajectories from each “sky” fiber in the ETA frame. The images from each slit are subdivided into several tens of intervals along the dispersion and the positions of the intensity distribution peaks in the direction perpendicular to dispersion are searched in each interval. The portions where the number of peaks is not equal to 12 are discarded. The coordinates of the remaining points are fitted by a second-order polynomial. The resulting error of the determination of the position of fiber trajectories does not exceed 0.2 pixels (see Fig. 9a).

Search for lines in NEON frames is performed by identifying peaks in the intensity distribution in the spectrum integrated along the trajectory of the central “sky” fiber. The search for peaks can be performed both automatically and via cross correlation with the model spectrum of the He-Ne-Ar lamp constructed for each grating used. Then iterative search of line centers is performed in the spectra obtained by integrating along the remaining “sky” fibers—the coordinates determined from the previous spectrum are used as the initial approximation. The coordinates of each line determined via this procedure are approximated by a second-order polynomial.

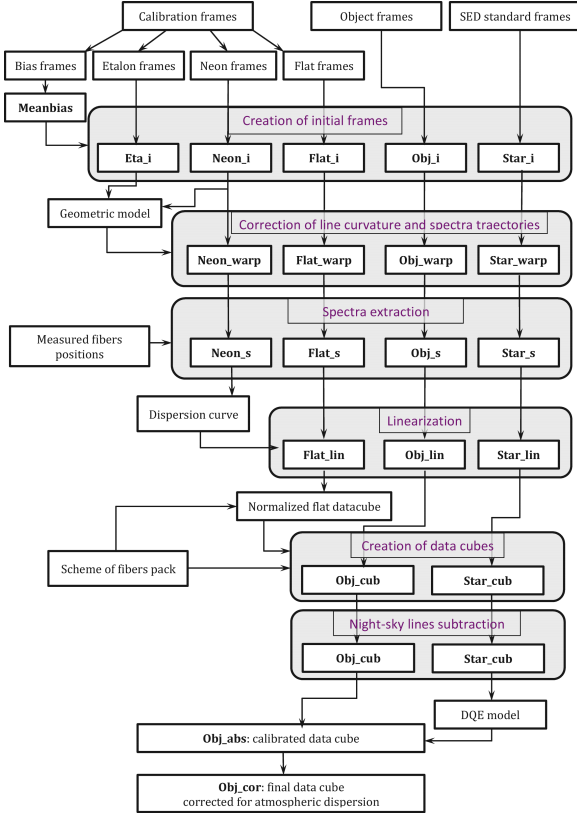


Fig. 8.— Block diagram of the data reduction procedure using IFURED package. The bold font is used to indicate the names of the files created at each stage of reduction.

The points of intersection of identified trajectories of “sky” fibers (the red lines in Fig. 9b) and the lines of the He-Ne-Ar lamp (the orange lines in Fig. 9b) are used as the grid points of the geometric model of 2D spectra (the magenta points in Fig. 9b). They are supplemented with a number of boundary points on each side of the frame obtained by extrapolating the resulting grid beyond the spectrum. These operations are followed by the correction of geometric distortions using WARP_TRI, which is a standard IDL procedure. Fig. 9c shows the result of correction for NEON.

3.3. Extraction of Spectra

In the resulting frames the flux from each fiber is not constrained to a single pixel along the slit but is scattered over several neighbouring pixels. The aim of the procedure of extraction of spec-

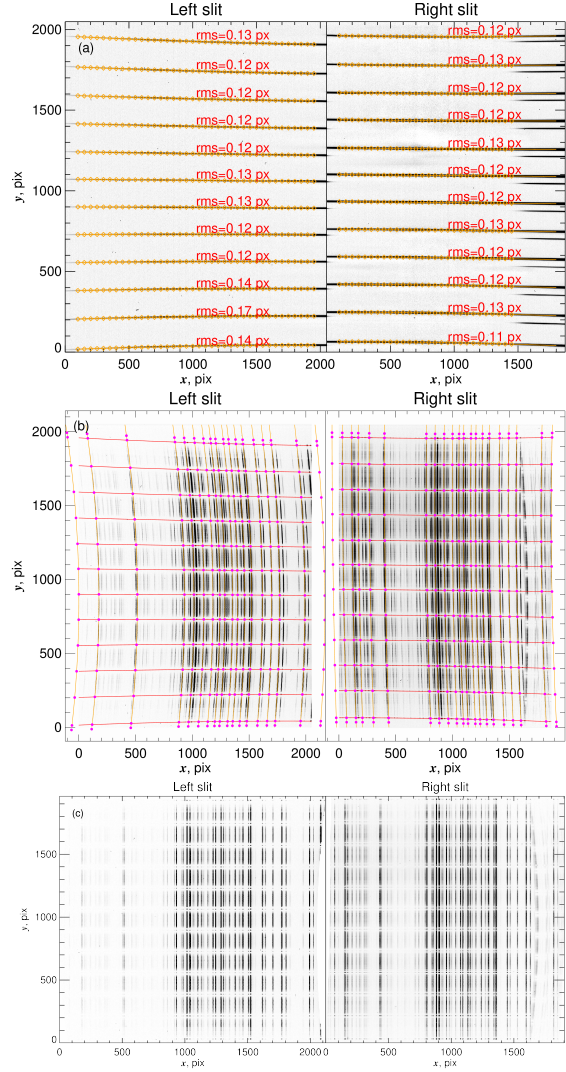


Fig. 9.— Illustration of the procedure of the correction of geometric distortions. The left and right panels show the results obtained for the left and right slits, respectively. (a)—Identification of trajectories of “sky” fibers in the ETA spectrum; the accuracy of the procedure for each fiber is indicated. (b)—The NEON spectrum, identified lines (orange) and trajectories of “sky” fibers (red), their intersection points (magenta). Extrapolation is performed beyond the observed spectrum. (c)—NEON after correction for geometric distortions.

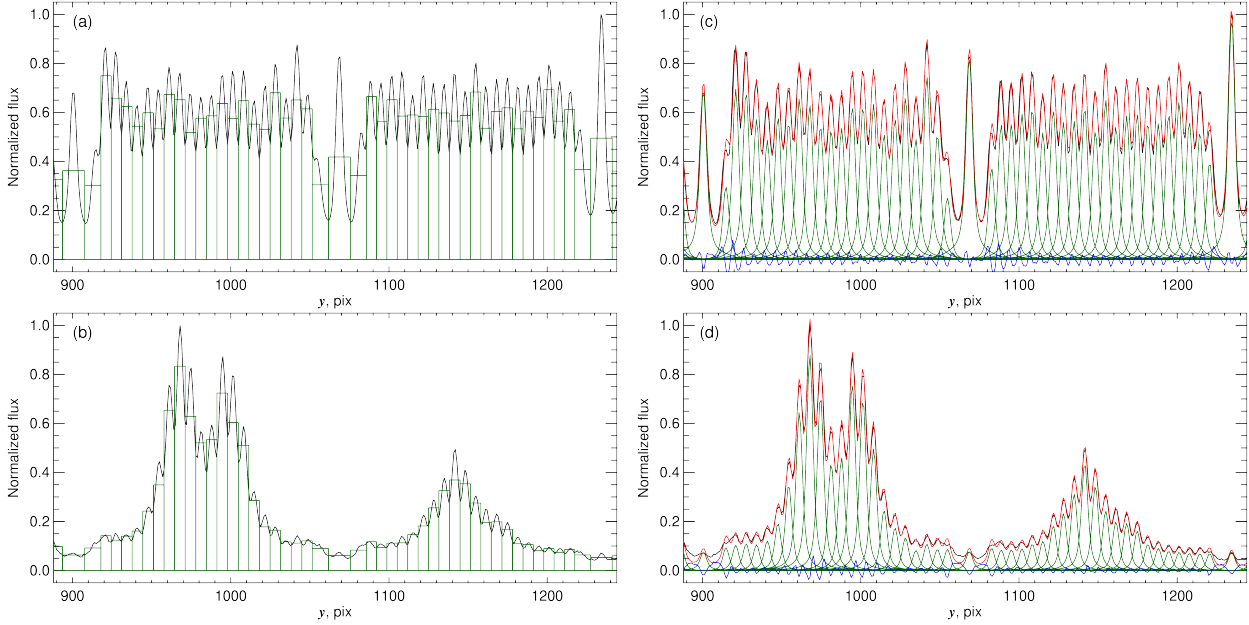


Fig. 10.— Distribution of normalized intensity across the dispersion direction in the FLAT (a, c) and OBJ (b, d) spectra from the right slit. The widths and areas of rectangles in panels (a, b) correspond to the size of the integration domain and the flux from each fiber in the case of simple extraction of spectra. The green lines in panels (c, d) show the intensity distributions from each fiber, the red line shows the integrated model spectrum, and the blue line shows the difference between the observed and extracted intensity distributions for optimum extraction.

tra is to obtain the integrated spectrum from each fiber.

To accomplish this stage we use the file containing laboratory measurements of the positions of all fibers along each slit. Given the ETA frame coordinates of the “sky” fibers identified at the previous stage we use interpolation to compute the coordinates of the centers of the trajectories of all fibers in the FLAT frame.

Extraction of spectra in IFURED program can be performed in two ways. Simple extraction consists in integrating the flux within rectangular aperture around the identified centers of the fiber trajectories in the 2D spectrum. The halfwidth of the aperture is set equal to half the distance between the adjacent peaks. Fig. 10a,b illustrates the application of this technique to the FLAT and OBJ spectra. The areas of rectangles in this figure corresponds to the integrated flux in the aperture.

The shortcoming of simple extraction method is that it does not account for scattering of light from each fiber: point spread functions (PSF)

of individual fibers overlap. Part of the scattered light is a result of scattering in the optics of the instrument. Unlike MPFS, where scattering amounts to 10–15% because of the use of a mirror-lens camera, scattering in SCORPIO-2 does not exceed 2%, which is achieved as a result of application of AR coatings to optical surfaces and the use of volume phased holographic gratings. We take into account scattering via the method of optimum extraction. To this end, we first construct a model of the flux distribution from fibers along the slit. The scattering function at the exit of the fiber can be described quite well by the Voigt function, which has extended and low-contrast wings. The width of the PSF of each fiber is determined by fitting the intensity distribution along the slit in FLAT frames. To take into account the variation of the PSF width, this procedure is applied to several dozen sections along the slit at various wavelengths. The inferred PSF widths of each fiber are interpolated over the entire spectral range and fixed for all data types. Final extraction of spectra

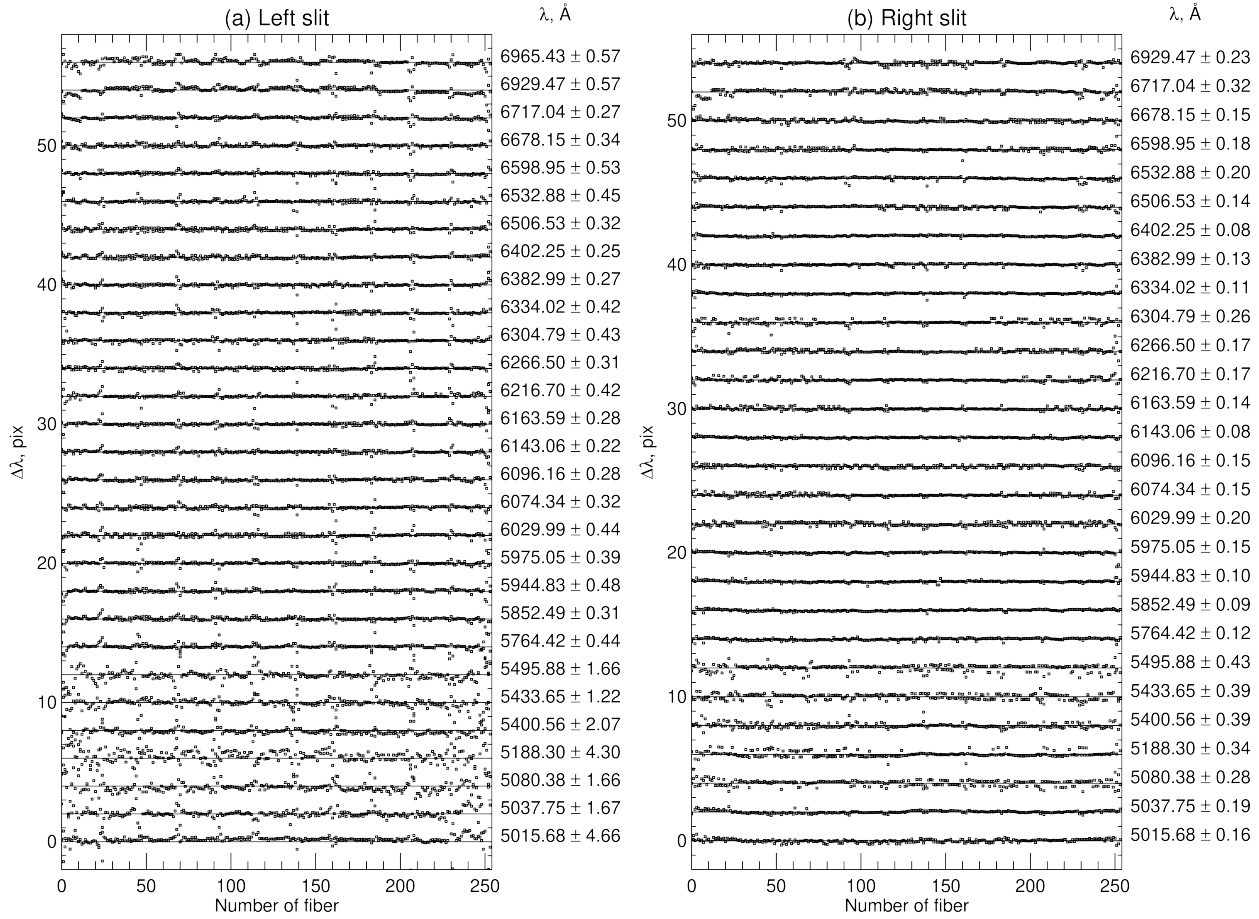


Fig. 11.— Distribution of deviations of the positions of identified lines of the He-Ne-Ar lamp from the laboratory wavelengths after linearization procedure along the (a) left and (b) rightslits.

for all data types is performed by fitting 254 Voigt profiles with fixed centers and widths to the intensity distribution along the slit for each pixel along the dispersion. The only free parameters are the intensities of all profiles. Fig. 10c,d illustrates the application of optimum extraction procedure to FLAT and OBJ data.

3.4. Linearization

The data obtained are wavelength calibrated (linearization of the spectrum) using the calibration spectrum of the He-Ne-Ar lamp (NEON). The positions of lines in the NEON frame are determined using the cross-correlation method with the preconstructed model emission spectrum for each employed grating. The positions of identified lines are used to construct the dispersion curve—the dependence of the wavelength in the spectrum on the coordinate in the frame. IFURED allows setting the degree of the polynomial used to fit the curve both along the dispersion axis and along the slit to correct for eventual geometric distortions. The resulting dispersion curve is used to linearize the entire data set.

Fig. 11 shows the deviations of the positions of identified lines of the He-Ne-Ar lamp from the laboratory wavelengths after applying the linearization procedure using the dispersion curve in the form of a third-order polynomial along the dispersion and second-order polynomial along the slit. Note that the large scatter in the blue part of the spectrum is due to low signal-to-noise ratio in this part of the spectrum, which, in turn, is due to the short exposure of the NEON frame in the data set used for this demonstration.

3.5. Flatfield Normalization and Creation of Data Cubes

Correction of the observed spectra for nonuniform transmission of each spectrum due to optical vignetting across the field of view and variations of the fiber transmission is a necessary stage in the data reduction. By default IFURED uses to this end the FLAT “flatfield” frame — the spectrum of the (quartz or LED) flatfield lamp taken with the SCORPIO-2 calibration system (Afanasiev et al. 2017). Nonuniform transmission is corrected after assembling data cubes.

The data cube is a three-dimensional array with

two space coordinates and one spectral coordinate. They are assembled in accordance with the given scheme of fiber packing in the IFU unit. Linearized spectra from the left and right slits form the upper and lower halves of the 22×24 pix² data cubes. The top and bottom rows are made of night-sky spectra (NS). These rows are formed from the data of fewer fibers than pixels and therefore to ensure uniform their filling the spectra from the NS are written to every second pixel in the row and the intensity distribution in other pixels is replaced by averaged spectra of the neighboring pixels.

The the wavelength-smoothed FLAT data cube is formed. The FLAT spectrum is not flat and therefore FLAT has to be normalized to the spectral brightness distribution of the flat field. We determine it as the brightness distribution averaged over all spectra in the cube. Every smoothed spectrum in the FLAT cube is then normalized to the brightness distribution of the flat field. All other data cubes are corrected for nonuniform illumination by dividing them by the normalized 3D flatfield spectrum described above.

In the cases where we obtain twilight spectra SUNSKY, we can use them to validate the quality of the correction of nonuniformities in the data cubes using normalized FLAT—possible errors are due to the violation of the telecentricism condition in the calibration path. In this case the corrected SUNSKY cube is used to produce the secondary normalized flatfield (in accordance with the above algorithm) by which to divide the OBJ and STAR data cubes.

3.6. Subtraction of Night-Sky Lines

To subtract the night-sky spectrum from all OBJ and STAR frames the spectra from “sky” fibers are used that correspond to empty areas aside from the observed object. In the assembled data cubes they form the upper and lower rows for the left and right slits, respectively. For each column in the data cube the spectrum from the “sky” fiber from the same column is used; the upper and lower rows are used for the upper and lower half, respectively.

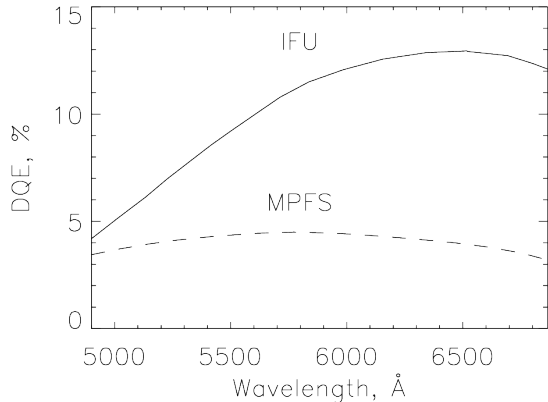


Fig. 12.— Measured quantum efficiency of IFU SCORPIO-2 with VPHG940@600 grating. For comparison the dashed line shows the quantum efficiency of MPFS spectrograph with 600 mm^{-1} reflective diffraction grating.

3.7. Flux Calibration, Correction of the Atmospheric Extinction and Dispersion

Calibration of fluxes in terms of energy units is performed in the standard way—the observed integrated spectrum STAR of one of the spectrophotometric standards (e.g., adopted from the list published in Oke 1990) is compared to the known spectral energy distribution for this object. Given the measured coefficients of atmospheric extinction for the Special Astrophysical Observatory of the Russian Academy of Sciences (Neizvestny 1983; Kartasheva & Chunakova 1978), we can compute the extinction at the zenith angle corresponding to the observed standard. After that it is easy to directly estimate the expected number of photons from the spectrophotometric standard incident onto the telescope mirror and compare the result with the observed values at different wavelengths. The resulting quantum efficiency curve (DQE) (see Fig. 12) is used to take into account the spectral response of the instrument. The fluxes in the observed OBJ data cube are then multiplied by the transformation coefficient from counts to energy units computed from the STAR cube and also by the normalization coefficient taking into account the difference the zenith angles of the object and spectrophotometric standard and the times of their exposures. As is ev-

ident from the figure, $\text{DQE} \sim 13\%$ at 6000 Å in the IFU mode with VPHG940@600 grating. For the same grating our measurements in the longslit mode yield $\text{DQE} \sim 42\%$ (Afanasiev & Moiseev 2011). The result of a comparison of the LS and IFU modes shows that in the latter case the quantum efficiency of the instrument decreases by a factor of about 3. This conclusion is consistent with our estimates mentioned in Section 2.2, where we conclude that the quantum efficiency decreased by a factor of 2.5. For comparison, the dashed line in the same figure shows the DQE curve for MPFS spectrograph obtained with a 600 lines mm^{-1} grid. Note that we used the data obtained with a similar dispersion: 1.2 Å mm^{-1} for IFU and 1.42 Å mm^{-1} for MPFS. The maximum DQE for MPFS is of about 4.5%, whereas this is almost three times less than our achieved efficiency in the IFU mode. The efficiency of the IFU mode when operating with a higher dispersion (VPHG with a modulation of 1800 and 2300 mm^{-1}) decreases to about 6%.

The last stage of data reduction is the correction for atmospheric dispersion. To this end, the wavelength dependence of the position of the barycenter of the OBJ object in the field of view is constructed, which is used to correct the OBJ file. At zenith angles smaller than 50° the corresponding offsets do not exceed one pixel throughout the entire spectral range.

3.8. Analysis of Reduced Data

In addition to the reduction procedures described above IFURED also includes tools for data visualization and basic analysis. Fig. 13 shows the image of Mrk 78 galaxy in the continuum obtained from the assembled data cube, and also an example of the spectrum corresponding to a pixel located near the center of the galaxy. As is evident from the figure, the use of VPHG940@600 grating with IFU allows studying emission lines in the wavelength interval from $\text{H}\beta$ to $[\text{NII}] 6584 \text{ Å}$ (up to $[\text{SII}] 6731 \text{ Å}$ in the case of closer objects).

To illustrate the use of IFURED or basic analysis of the data, Fig. 14 shows the flux and radial-velocity maps of Mrk 78 galaxy in $\text{H}\alpha$, $[\text{NII}] 6584 \text{ Å}$ $[\text{OIII}] 5007 \text{ Å}$ and $\text{H}\beta$ lines. These images were acquired by approximating each emission line by a single-component Gaussian profile and underlying second-order polynomial describing the continuum via MPFIT (Markwardt 2009) procedure.

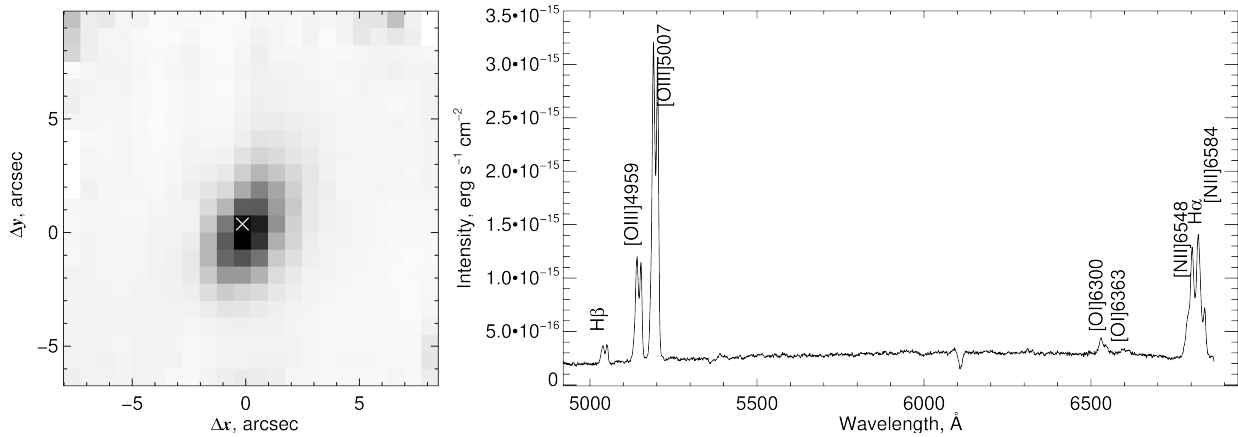


Fig. 13.— Integrated image of Mrk 78 in the continuum. The right panel shows, by way of an example, the spectrum corresponding to the pixel marked by the red cross, and also indicates the identification of observed bright emission lines.

The [OIII] 4959,5007Å and [NII] 6548,6584Å line doublets can in this case be approximated by two components with a fixed separation and the same FWHM. The contours in the figure show the continuum brightness distribution.

In the maps presented here two bright regions in Mrk 78 can be seen in all emission lines, whereas in the continuum the galaxy mostly shows up between these regions. The $H\alpha$ velocity field shows regular rotation, and its distortion in the [OIII] line is indicative of noncircular motions.

Note, however, that in the case of Mrk 78 a single-component Gaussian profile fit gives only a rough idea about the kinematics and morphology of gas in the galaxy. Previous observations of Mrk 78 revealed complex kinematics of ionized gas, which manifests itself in observed multicomponent emission-line profiles (Whittle & Wilson 2004). Bifurcation of line profiles can also be clearly seen in our Fig. 13. A detailed analysis of the kinematics and gas ionization mechanisms in Mrk 78 galaxy requires a special paper.

4. CONCLUSION

The multimode SCORPIO-2 spectrograph designed for the 6-m telescope includes an IFU unit with a lens raster meant for field spectroscopy. Here are the main points:

1. The operation principle of IFU—a square raster made of microlenses with $23\times$ magni-

fying optics.

2. The lens raster contains 22×22 square microlenses, each with the size of 2 mm; the image scale is $0''.75/\text{lens}$, and the size of the field of view is $16''.5 \times 16''.5$.
3. Optical fibers reform micropupil images into two pseudoslits located at the IFU collimator entrance. Each slit contains 254 fibers (242 fibers from the object + 12 fibers from the sky background). At the spectrograph output two arrays is formed, each consisting of 254 spectra.
4. A set of volume phased holographic gratings (VPHG) provides the spectral interval 4600–7300 Å and a resolution of $\lambda/\delta\lambda$ from 1040 to 2800 in the IFU mode.
5. The quantum efficiency of the IFU mode is 6–13% depending on the grating employed, which, all other conditions being equal, exceeds the efficiency of MPFS by a factor of about three.
6. We developed IFURED software package for primary reduction of the data.

The IFU mode in SCORPIO-2 spectrograph is meant for field spectroscopy of central regions in galaxies in the $H\beta$ and $H\alpha$ lines, for diagnosing the conditions of gas ionization and studying of its kinematics. We also plan to study the stellar component in central parts of galaxies in absorption

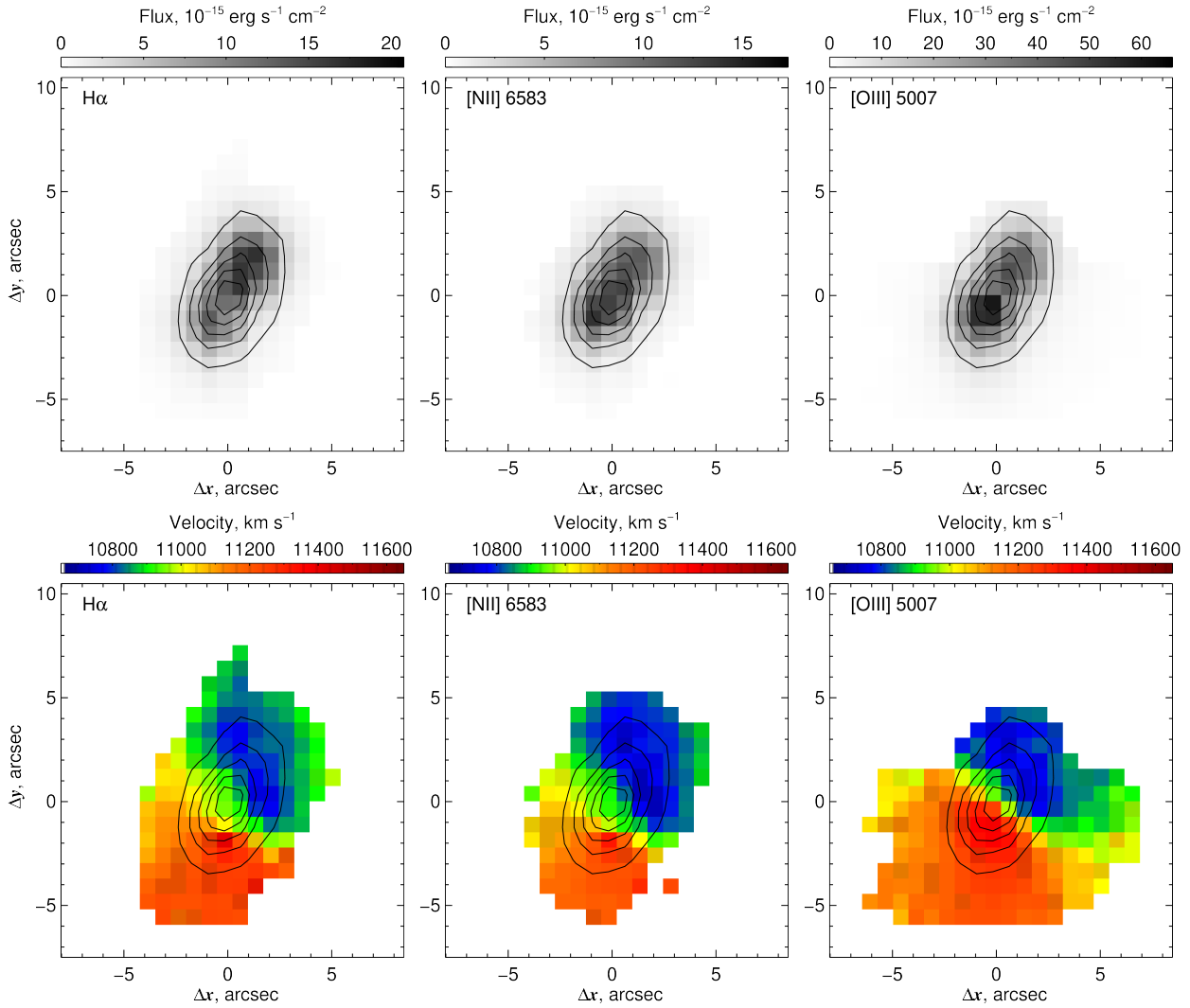


Fig. 14.— Result of fitting H α , [NII] 6584 Å and [OIII] 5007 Å lines (left to right) by a single-component Gaussian profile and continuum. Top to bottom: distribution of line flux and radial-velocity fields. The contours show the brightness distribution in the continuum.

lines—the chemical composition, stellar velocity dispersion and stellar velocity field. We consider this to be an extra mode in addition to photometry, long-slit spectroscopy, and field spectroscopy with a Fabry–Perot interferometer for observing extended objects with SCORPIO-2.

We are grateful to R. I. Uklein for measuring flexures on the 6-m telescope of the Special Astrophysical Observatory of the Russian Academy of Sciences and to the administration of the Special Astrophysical Observatory of the Russian Academy of Sciences for allocating observational time for technical tests. This work was supported by the Russian Science Foundation (project no. 17-12-01335).

REFERENCES

- V. L. Afanasiev, S. N. Dodonov, V. V. Vlasyuk, and O. K. Silchenko, Preprint of Spec. Astrophys. Obs. of RAS, Nizhnij Arkhyz, #54 (1990).
- V. L. Afanasiev, V. V. Vlasyuk, S. N. Dodonov, and S. V. Drabek, *Multipupil Spectrograph MPFS. User's Manual* (1995)
https://serv.sao.ru/hq/lsvfo/devices/mpfs/MPFS_V1/MPFS_V1.html
- V. L. Afanasiev, S. N. Dodonov, and A. V. Moiseev, in *Stellar Dynamics: from Classic to Modern*, Edited by L. P. Ossipkov and I. I. Niki-forov, p. 103. (2001)
- V. L. Afanasiev and A. V. Moiseev, *Astronomy Letters* **31**, 194 (2005).
- V. L. Afanasiev and A. V. Moiseev, *Baltic Astronomy* **20**, 363 (2011).
- V. L. Afanasiev, V. R. Amirkhanyan, A. V. Moiseev, et al., *Astrophysical Bulletin* **72**, 458 (2017).
- S. Arribas, P. M. Gray, R. Terlevich, et al., *Ap&SS* **171**, 293 (1990).
- R. Bacon, G. Adam, A. Baranne, et al., *A&AS* **113**, 347 (1995).
- R. Bacon, Y. Copin, G. Monnet, et al., *MNRAS* **326**, 23 (2001).
- S. C. Barden, J. A. Arns, W. S. Colburn, and J. B. Williams, *PASP* **112**, 809 (2000).
- G. Courtés, *Astrophysics and Space Science Library* **92**, 123 (1982).
- T. A. Kartasheva and N. M. Chunakova, *Astrofizicheskie Issledovaniia Izvestiya Spetsial'noj Astrofizicheskoy Observatorii* **10**, 44 (1978).
- H. Kogelnik, *The Bell System Technical Journal*, **48**, 2909 (1969).
- F. Laurent, F. Henault, E. Renault, et al., *PASP* **118**, 1564 (2006).
- C. B. Markwardt, *ASP Conf. Ser.* **411**, 251 (2009).
- G. J. Murray, J. R. Allington-Smith, R. Content, et al., *Proc. SPIE* **4841**, 1750 (2003).
- S. I. Neizvestny, *Astrofizicheskie Issledovaniia Izvestiya Spetsial'noj Astrofizicheskoy Observatorii* **17**, 26 (1983).
- J. B. Oke, *AJ* **99**, 1621 (1990).
- M. M. Roth, A. Kelz, T. Fechner, et al., *PASP* **117**, 620 (2005).
- C. Sandin, T. Becker, M. M. Roth, et al., *A&A* **515**, A35 (2010).
- C. Vanderriest, G. Courtés, and J. Donas, *Journal of Optics* **15**, 237 (1984).
- M. Whittle and A. S. Wilson, *AJ* **127**, 606 (2004).

Translated by A. Dambis